A Numerical Kirchhoff Simulator for GNSS-R Land Applications

Weihui Gu, Haokui Xu, and Leung Tsang[*]

Abstract—A distinct feature of GNSS-R land reflectometry is that random rough surfaces are superimposed on many levels of elevations. The rms elevations are in tens of meters which are many times larger than the microwave wavelengths at GNSS frequencies. Such multiple elevations were not considered in the coherent model nor the incoherent model. In this paper, we studied the electromagnetic scattering of this new rough surface scattering problem using Kirchhoff integral as first-principle. A numerical Kirchhoff simulator is developed to calculate the electromagnetic scattering and the power ratio in the specular direction. The integration is carried out over a footprint of 10 km by 10 km with the specular point as the center. In integration the surface discretization is as small as 2 cm by 2 cm so that a total of 2.5×10^{11} patches are used. Parallel computing is implemented requiring a moderate amount of computer resources. The results of the power ratio of the numerical Kirchhoff simulator differ from the results of both the coherent model and incoherent model. The results show that the phase of the first Fresnel zone is random, and the power contributed by the first Fresnel zone is a small fraction of that over the 10 km by 10 km. The power ratios of the numerical Kirchhoff simulations are much larger than that of the incoherent model and smaller than the coherent model for small RMS heights. The results show that the multiple elevations in land have large effects on GNSS-R specular reflections.

1. INTRODUCTION

Signals of opportunity from Global Navigation Satellite Systems (GNSS), such as Global Position System (GPS), GLONASS, Galileo and TechDemoSat, have been used for a variety of Earth remote sensing applications [1–6] including ocean altimetry, retrieval of oceansurface wind speeds, and monitoring the soil moisture. GNSS-R are signals of opportunities as only receivers are required unlike monostatic and bistatic radars. The proposal of using GNSS signals to perform scatterometry was first made in 1988 [1]. Five years later GNSS-Reflectometry (GNSS-R) was used for mesoscale ocean altimetry [2]. The first experiment demonstrating oceansurface wind sensing by GNSS-R was reported in 1998 [3]. The feasibility of space borne GNSS-R from ocean, ice and land surfaces were demonstrated by UK-DMC [7]. An in-depth review of development of GNSS-R technology can be found in [8].

The Cyclone Global Navigation Satellite System (CYGNSS) constellation was launched by the National Aeronautics Space Administration (NASA) in 2016 [9]. CYGNSS measures GPS signals over both ocean and land surfaces at a 10–15 km spatial resolution with an average revisit time of 3–7 hours. CYGNSS has been successful in monitoring near ocean surface wind speeds [10, 11]. Recent studies have demonstrated the sensitivity of the spaceborne GNSS signals to soil moisture [12, 13]. The availability of the GNSS-R data over land has motivated investigations for a variety of land applications [8, 14–16]. A distinct difference in GNSS reflectormetry is that the scattered direction is in the specular direction.

In the past, the studies of electromagnetic wave scattering by random rough surface were conducted for profiles with a single elevation. Usually, the mean height equals, zero and the rms height is smaller

than or up to 1 or 2 wavelengths. A distinct feature of the land scattering problem for GNSS-R from past problems is that the random rough surfaces of microwave centimeter scale are superimposed on many levels of elevation. The rms elevations are in meters and tens of meters which are many times larger than the microwave wavelength at GNSS frequencies. Such scattering problems of multiple elevations have not been studied in the past. Two models have been used for GNSS-R land applications. The coherent model [17] and incoherent model [18], both are based on solutions from past rough surface scattering problems. The coherent model is based on the Fresnel zone concept that assumes a single elevation of rough surface scattering. It assumes a small centimeters rms height about a flat surface. The phases of the scattered waves then alternate between 0 and pi between adjacent Fresnel zones. Such Fresnel zones cannot be the case for land surfaces with DEM of tens of meters as a height of 5 cm already gives a phase shift of pi. The incoherent model treats GNSS-R as a special case of bistatic incoherent radar. Although GNSS-R land measurements have been taken over the last few years, it is difficult to resolve the issues because the reflected power comes from an area of 10 km by 10 km with large variations of elevations. A key point is how the large variations of elevations affect the specular reflections.

In this paper, we studied the electromagnetic scattering of the rough surface scattering problem of multiple elevations using Kirchhoff integral as the first-principle. A numerical Kirchhoff simulator is developed to calculate the electromagnetic scattering and the power ratio in the specular direction. The integration is carried out over a footprint of 10 km by 10 km with the specular point as the center. In integration the surface discretization is as small as 2 cm by 2 cm so that a total of 2.5×10^{11} patches are used. Using the procedure, we keep track of the phase and amplitude of the scattered field from each 2 cm by 2 cm. Parallel computing is implemented requiring a moderate number of computer resources. Frequency averaging is taken to smooth out the fluctuations due to random rough surface scattering. The simulations of rough surface scattering are carried out using CYGNSS geometries at the frequency of 1.575 GHz and using DEMs. The results of power ratio of the numerical Kirchhoff simulator differ from the results of both the coherent model and incoherent model at small rms heights. The results show that the phase of the scattered waves from the first Fresnel zone are random, and the power contributed by the first Fresnel zone is a small fraction of the power ratio of the 10 km by 10 km. The power ratios of the numerical Kirchhoff simulations are much larger than that of the incoherent models and smaller than the coherent model for small RMS heights.

In Section 2, we review the coherent and incoherent models. In Section 3, we describe the numerical Kirchhoff simulator and computer resources. Section 4 presents simulation results and discussions.

2. COHERENT AND INCOHERENT MODELS

The geometrical configuration of the GNSS-R is shown in Figure 1. The signal is sent from the transmitter on the GNSS satellite at height h_t and received by a receiver at quasi-specular direction at height h_r. The horizontal distance between the transmitter and receiver is L. The specular point is set at the origin $(0, 0, 0)$. R_t is the distance from transmitter to the specular point, and R_r is the distance from the receiver to the specular point. Based on signal processing of the GNSS-R receiver, the powers received are from the waves that are scattered from an area of 10 km by 10 km.

2.1. Coherent Model and Incoherent Model

In the coherent model, the ratio of received power P_r to the transmitted power P_t is

$$\frac{P_r}{P_t} = \frac{G_t}{4\pi \left(R_{pt} + R_{pr}\right)^2} \frac{G_r \lambda^2}{4\pi} \left|R_{lr}\right|^2 e^{-4k^2 h^2 \cos^2 \theta} \tag{1}$$

where G_t and G_r are the gains of the transmitter and receiver, respectively; R_{lr} is the Fresnel reflection coefficient for land surface; l, r stands for left and right hand circular polarizations, respectively; k is the propagation constant; θ is the incident angle; and h is the roughness of the surface. The coherent model is from past model of rough surface scattering which assumes a single elevation, and the contributions arise from Fresnel zones [20]. The attenuation caused by the surface roughness is the exponential term $e^{-4k^2 h^2 \cos^2 \theta}$. In the appendix, this formula in Equation (1) is derived rigorously by using plane wave
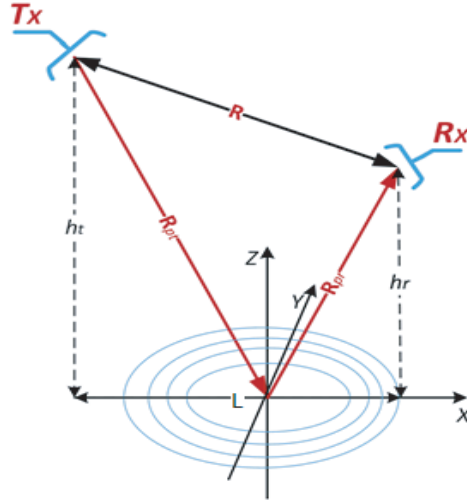
Figure 1. Geometrical configuration of GNSSR.

expansions of spherical waves, taking ensemble average of the scattering waves in the presence of random roughness and the method of stationary phase.

The incoherent model is also based on past scattering model and treats the GNSS-R as a special case of bistatic radar scattering with the scattering angle in the specular direction. In the bistatic radar equation, the received power ratio is

$$\frac{P_r}{P_t} = \frac{G_t}{4\pi R_{pt}^2} \frac{1}{4\pi R_{pr}^2} \frac{G_r \lambda^2}{4\pi} \int \gamma dA \tag{2}$$

where γ is the bistatic scattering coefficient of incoherent waves. The formula in Equation (2) is proportional to surface area. Based on geometrical optics approximation [19–21], the bistatic scattering coefficient is

$$\gamma = \frac{|R_{lr}|^2}{2s^2} \tag{3}$$

where s is the RMS slope of the surface, and R_{lr} is defined previously under Equation (1). It is well known that surfaces with exponential correlation functions do not have RMS slope [21–24]. In the case of Gaussian correlation function, $s = \sqrt{2}h/l$, where l is the correlation length of the rough surface [21]. The incoherent model ignores the contributions of the coherent waves.

2.2. Comparisons of Coherent and Incoherent Model

In Figure 2, we plot the power ratio using coherent and incoherent models in Equations (1) and (2), respectively. The results are plotted as a function of RMS height h with correlation length $l = 14.1h$, based on Gaussian correlation function. The area is $A = 10\,\text{km} \times 10\,\text{km}$. The results show large differences of many decibels between the two models. At $h = 0\,\text{cm}$, the coherent model is 30 dB larger than the incoherent model. The two curves intersect at about $h = 4\,\text{cm}$. For larger RMS heights, the incoherent model gives a much larger power than the coherent model.

3. KIRCHHOFF SIMULATOR

3.1. Kirchhoff Integral

In this paper, we study the scattering of random rough surfaces with multiple elevations as a new rough surface problem by using the Kirchhoff integral as the first principle. From Huygen's theorem, the
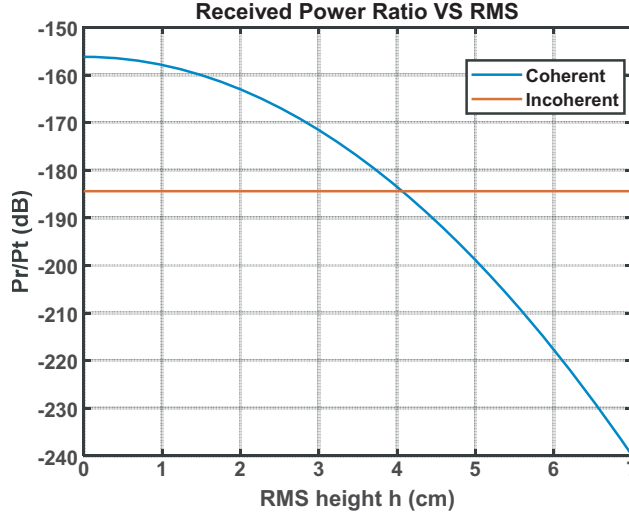
Figure 2. Power ratio of coherent and incoherent models as a function of RMS height, with $s = 0.1$, $A = 10\,\text{km} \times 10\,\text{km}$.

scattered field is calculated from the tangential electric and magnetic fields on the surface by [19]:

$$\bar{E}_s\left(\bar{r}\right) = \iint dS' \left[i\omega\mu \bar{\bar{G}}\left(\bar{r}, \bar{r}'\right) \cdot \hat{n}' \times \bar{H}\left(\bar{r}'\right) + \nabla \times \bar{\bar{G}}\left(\bar{r}, \bar{r}'\right) \cdot \hat{n}' \times \bar{E}\left(\bar{r}'\right) \right] \tag{4}$$

where $\bar{\bar{G}}$ is the dyadic Green's function; $\bar{E}$ and $\bar{H}$ are the electric and magnetic fields, respectively; and $\hat{n}'$ is the surface normal. With Kirchhoff approximation. The surface fields are approximated by using the tangent plane approximation.

We carry out integration of Equation (4) over a large area of $10\,\text{km}$ by $10\,\text{km}$ at microwave frequencies. Let the surface be discretized into patches, $\alpha = 1, 2, \ldots, N_M$, where subscript M stands for microwaves. The patch size is $2\,\text{cm}$ by $2\,\text{cm}$ to account for microwave roughness and microwave phase information. Thus 2.5×10^{11} microwave patches are used requiring parallel computations. The Dyadic green's function is

$$\bar{\bar{G}}\left(R\right) = \left[\left(\frac{3}{k^2 R^2} - \frac{3i}{kR} - 1 \right) \hat{k}\hat{k} + \left(1 + \frac{i}{kR} - \frac{1}{k^2 R^2} \right) \bar{\bar{I}} \right] \frac{e^{ikR}}{4\pi R} \tag{5}$$

where $R = |\bar{r} - \bar{r}'|$ is the distance from source point $\bar{r}'$ to observation point $\bar{r}$. Since both the transmitter and receiver are far away from the surface, far field approximation is applied to amplitude term. The phase term is kept intact to account for phase effects. The approximated dyadic Green's function is

$$\bar{\bar{G}}\left(R\right) \approx \left(\bar{\bar{I}} - \hat{k}\hat{k} \right) \frac{e^{ikR}}{4\pi R} \tag{6}$$

With the local orthonormal system $(\hat{p}_i \hat{q}_i \hat{k}_i)$ defined at each point on the surface,

$$\hat{q}_i = \frac{\hat{k}_i \times \hat{n}'}{\left| \hat{k}_i \times \hat{n}' \right|}$$

$$\hat{p}_i = \hat{q}_i \times \hat{k}_i$$

the surface incident field is decomposed into locally perpendicular and parallel polarization field. $\hat{n}'$ is the normal vector, and $\hat{k}_i$ is the incident vector at that point. Detailed derivations can be found in [19].

The result Kirchhoff integral is

$$\bar{E}_s(\bar{r}) = \frac{ik}{4\pi}\sqrt{\frac{P_t\eta_0}{2\pi}} \iint_{S'} d\bar{r}' \frac{e^{ik(R_{pt}+R_{pr})}}{R_{pt}R_{pr}} \left(\bar{\bar{I}} - \hat{k}_s\hat{k}_s\right) \cdot \bar{F}(\alpha,\beta) \tag{7}$$

$$\bar{F}(\alpha,\beta) = \sqrt{1+\alpha^2+\beta^2} \begin{bmatrix} (-1+R_h)\left(\hat{e}_i \cdot \hat{k}_i\right)\hat{q}_i + (1+R_v)\left(\hat{e}_i \cdot \hat{p}_i\right)\hat{n}\times\hat{q}_i \\ +\hat{k}_s \times [(1+R_h)(\hat{e}_i \cdot \hat{q}_i)]\hat{n}\times\hat{q}_i + (1-R_v)(\hat{e}_i \cdot \hat{p}_i)\left(\hat{n}_i \cdot \hat{k}_i\right)\hat{q}_i \end{bmatrix} \tag{8}$$

where R_h and R_v are Fresnel reflection coefficients for perpendicular and parallel polarizations. The notations follow [19].

3.2. Fresnel Zones

We briefly review the concepts of Fresnel zones which are later shown to be inadequate for rough surfaces with many elevations of tens of meters. The Fresnel zone describes how a flat surface contributes to the total scattered field when a surface is illuminated by a point source as shown in Figure 1. The Fresnel zone denotes the phase term of the integrand by integer multiples of π. Let the distance of direct transmission from transmitter to receiver be R, and the total propagation distance of a reflected signal from the surface is $R_{pt} + R_{pr}$. The path difference δd between the signals from two different paths is

$$\delta R = R_{pt} + R_{pr} - R \tag{9}$$

Noting that R is a constant, for a given δR, the corresponding loci are ellipses on XY plane [20]. Let δR_0 be the path difference of reflection from the specular point, if δd increases from δR_0 in step of $n\lambda/2$

$$\delta R = \delta R_0 + n\lambda/2 \tag{10}$$

a family of ellipses are drawn, as shown in Figure 3. The heights of transmitter and receiver used are $h_t = 2.02 \times 10^7$ m and $h_r = 5 \times 10^5$ m, and the horizontal distance between them is $L = 6.8 \times 10^6$ m. Along the x direction, the semi-major axes of the first few Fresnel zones are shown in Table 1.

Let a_n be the semi-major axes of the nth ellipse, then the width of the nth Fresnel zone is $W_n = a_n - a_{n-1}$. In Figure 4, the X axis represents the distance from center to the edge, and Y

Table 1. Semi-major axes of first few Fresnel zone.

nth Fresnel zone	1	2	3	4	5
a_n (m)	337.23	476.91	584.09	674.45	754.06
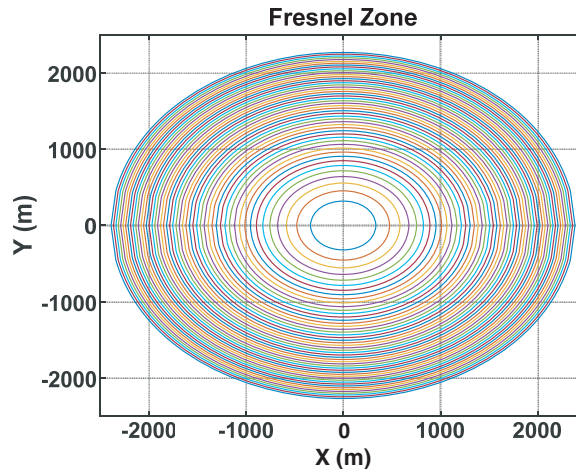
Figure 3. Fresnel Zone with $h_t = 2.02 \times 10^7$ m, $h_r = 5 \times 10^5$ m, $r = 6.8 \times 10^6$ m.
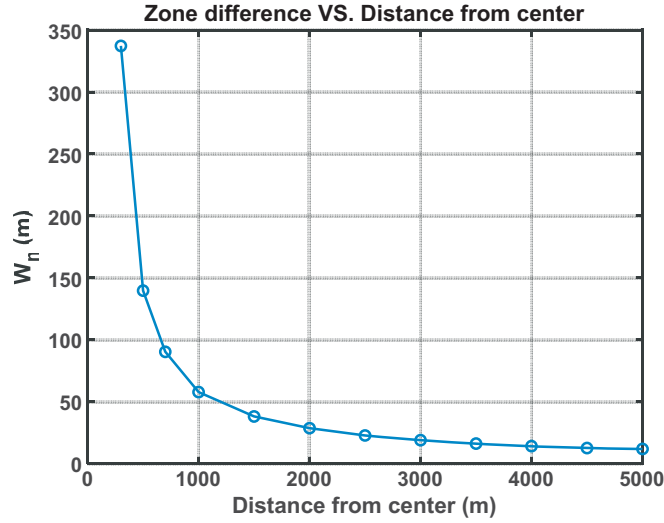
Figure 4. Semi-major axes difference of Fresnel zone.

axis is W_n. It shows that the width of Fresnel zones decreases from 336 m at center to 11 m at 5 km away from the center.

3.3. Frequency Averages

In the simulations in this paper, frequency averages are taken to average the fluctuations. Suppose that there are two different points a and b on the surface with total distance $R_{pt} + R_{pr}$ being d_a and d_b, respectively. The phase difference of the two points at two different frequencies is

$$\Delta\phi_0 = k_0 (d_a - d_b) \tag{11}$$
$$\Delta\phi_1 = k_1 (d_a - d_b) \tag{12}$$

The phase difference of the two frequencies is

$$\Delta\phi_d = \Delta\phi_0 - \Delta\phi_1 = (k_0 - k_1)(d_a - d_b) \tag{13}$$

For a 10 km by 10 km area, $\Delta d = (d_a - d_b)$ can be a large number which results from both the location (horizontal) and elevation difference. For a 10 km by 10 km flat surface, the maximum Δd is 44 m, which indicates a small difference in frequency and can create a large phase difference. We rewrite

$$\Delta\phi_d = \frac{f_0 - f_1}{f_0} \frac{2\pi (d_a - d_b)}{\lambda_0} = \frac{\Delta f}{f_0} \frac{2\pi \Delta d}{\lambda_0} \tag{14}$$

Let $\Delta d = 44$ m, $\Delta\phi_d = \frac{\pi}{2}$, the corresponding $\Delta f = 1.7$ MHz. Frequency averages with sampling $\Delta f = 0.2$ MHz are used for cases that have large height variation.

$$P_{mf} = \frac{1}{N} \sum_{i=1}^{N} P_i(f_i) \tag{15}$$

Frequency averages are taken over 10 MHz bandwidth.

3.4. Land Surface Profile Descriptions of DEM and Microwave Roughness

The land surface is characterized by digital elevation model (DEM). We describe the height function profile $f(x, y)$ as follows:

$$f(x, y) = f_{DEM}(x, y) + f_{mr}(x, y) \tag{16}$$

where $f_{DEM}(xy)$ is the elevation height based on DEM. The second term is random rough surface height f_{mr} where subscript mr stands for the microwave roughness. The DEMs are tens of meters.

Without the DEM, the problem reduces to that of the past rough surface scattering problem with a single elevation. The DEM data are from Advanced Space borne Thermal Emission and Reflection Radiometer (ASTER) Global Digital Elevation Model version 2 (GDEM2). The ASTER GDEM2 was released by NASA and METI Japan in mid-October 2011, which covers the land surface between 83°N and 83°S using 22702 1°×1° tiles. Each 1°×1° tile is composed of 3601 by 3601 pixels with patch size approximately 30 m × 30 m at the equator. The pixel size varies with longitude and latitude and can be calculated through Universal Transverse Mercator conformal projections. The small-scale surface height f_{mr}, with respect to DEM elevation height, is assumed to be a stochastic process which is characterized by roughness h and correlation functions [21].

Table 2. Phase shift of height different δd.

$Phase(2kd\cos\theta_i)$	35.93°	179.67°	359.36°
δd (cm)	1	5	10

In the DEM data, an elevation of d_i is given for the i patch, and $i = 1, 2, \ldots, N_D$, where N_D is the number of DEM patches. Note that we use the Roman numeral i to denote the DEM patch and use the Greek index α for microwave patches. The raw elevation height d_i is rounded to the nearest meter. A height difference of merely 10 cm will give a round trip phase shift of 2π, as shown in Table 2. We find that rounding the DEM to 1 meter tends to give a bias to the phase. Thus, a noise term n_i is add to the raw DEM data. For (x, y) on the i patch

$$f_{DEM}(x,y) = d_i + n_i \tag{17}$$

where d_i is the raw data given by DEM, and n_i is the Gaussian random variable of zero mean and a standard deviation of 10 cm. Note that $f_{DEM}(x,y)$ is constant for each patch, meaning that every DEM patch is assumed to be flat. We call $f_{DEM}(x, y)$ by $f_{DEM,raw}$ if the noise term n_i is set to zero.

3.5. Computation Resources

The computation in this paper is performed on FLUX, which is the shared Linux based high performance computing cluster available to all researchers at the University of Michigan. The standard hardware of Flux is:

(i) 109 Haswell architecture compute nodes, each configured with 24 cores (two 12-core 2.5 GHz Intel Xeon E5-2680v3 processors) and 128 GB RAM.

(ii) 124 Ivybridge architecture compute nodes, each configured with 20 cores (two 10-core 2.8 GHz intel Xeon E5-2680v2 processors) and 96 GB RAM.

(iii) 139 Sandybridge architecture compute nodes, each configured with 16 cores (two 8-core Intel Xeon E5-2670 processors) and 64 GB RAM.

(iv) 88 Nehalem architecture computer nodes, each configured with 12 cores (two 6-core 2.67 GHz Intel Xeon X5650 processors) and 48 GB RAM.

All the standard computer nodes are treated identically for purposes of Flux allocations and job scheduling.

Simulation code is written in MATLAB and will be converted in the future into C for better computation performance. Computation requirements for a single frequency are shown in Table 3.

Table 3. Computation resource used for different patch sizes.

Patch size	Number of patches	Cores used	RAM used	Time used (hours)
2 cm × 2 cm	2.5×10^{11}	33	32 GB	40
5 cm × 5 cm	4×10^{10}	33	16 GB	7
8 cm × 8 cm	1.56×10^{10}	33	16 GB	4

4. RESULTS OF NUMERICAL KIRCHHOFF SIMULATOR

Numerical results are illustrated for three different types of surface profiles.

(i) Microwave random roughness on single elevation: $f(x,y)=f_{mr}(x,y)$;

(ii) DEM only: $f(x,y)=f_{DEM}(x,y)$;

(iii) Microwave roughness superimposed on DEM: $f(x,y)=f_{DEM}(x,y)+f_{mr}(x,y)$.

Profiles in (i) are used to show that the numerical Kirchhoff simulator will give results that agree with past rough surface models. Case (iii) profiles represent reasonable approximations of real life land surfaces

4.1. Microwave Roughness Only

We consider Gaussian rough surfaces with Gaussian correlation function [19]. The slope is $s = 0.1$, and RMS heights vary from 1 to 7 cm. For each case, we used only a single realization of 10 km by 10 km. The circles shown in Figure 5 are the KA simulator results. For small RMS height from 0 to 3 cm, the KA simulator results agree with the coherent model. Starting from 4 cm rms height, incoherent power starts to make significant contribution. At 4 cm rms height, coherent and incoherent models predict a power ratio of -184.4 dB while the numerical Kirchhoff simulator is 3 dB higher. At 5 cm rms height, the power ratio is dominated by incoherent effect. The fluctuations around incoherent model results are due to incoherent effect at large rms heights. The fluctuations are averaged by taking frequency averages within the bandwidth as discussed earlier. The coherent model assumes a single elevation with rms height less than 4 cm. There is no such terrain. The real land profiles, based on DEM, are with many elevations of meters and tens of meters. However, it is reasonable that the rms height at each elevation is of centimeters. Thus we study later in Figure 10 this problem of microwave cm rms heights superimposed on DEM of meters.
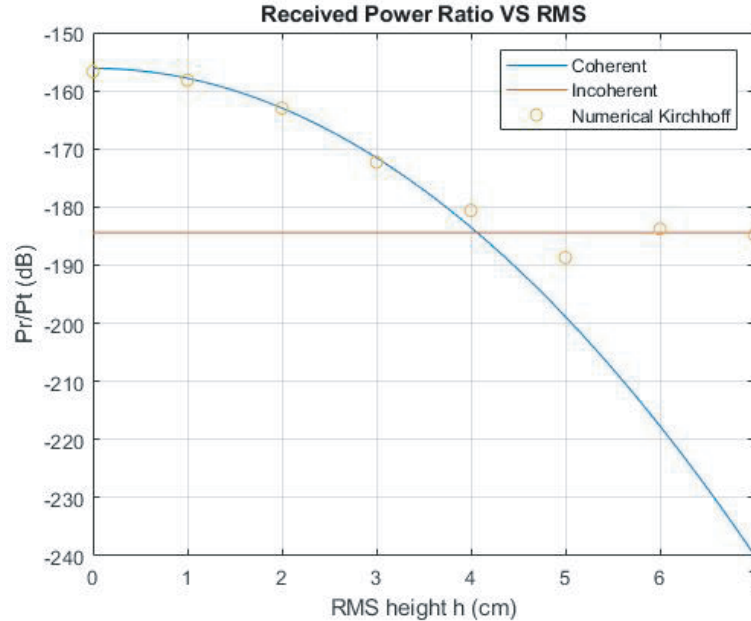
Figure 5. Single elevation results without DEM. The results with multiple elevations are shown in Figure 10.

4.2. DEM Only: $f(x,y)=f_{DEM}(x,y)$

A 10 km by 10 km area is chosen from 31°N to 32°N, 83°W to 84°W, where the DEM resolution is 26.5 m by 31.8 m. Thus the 10 km and 10 km surface corresponds to a 377×325 DEM patch array.
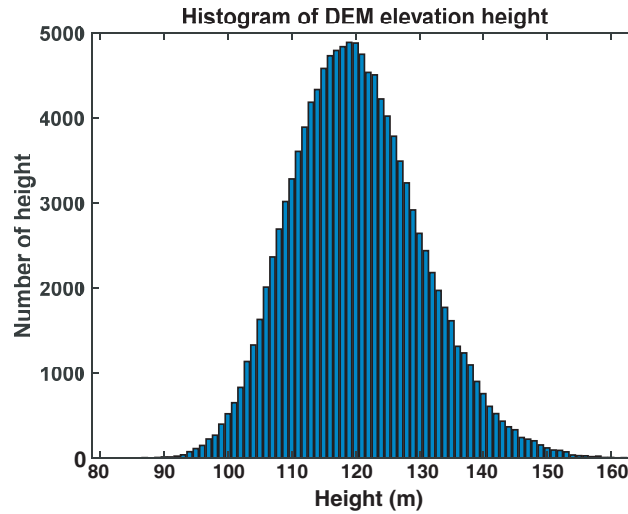
Figure 6. Histogram of DEM elevation height within 10 km and 10 km area.

Each patch has an elevation height $f_{DEM,raw}$. The histogram of the elevation height within the area is shown in Figure 6. The elevation height ranges from 80 m to 163 m; the mean height is 121.6 m; and the standard deviation is 10 m.

To avoid phase bias as discussed in Section 3.4, a random noise is added as shown in Equation (17). We choose the scattered field from the specular point as reference phase ϕ_0. The phase distributions of patches are plotted. The patch is drawn in yellow if the patch phase is within $\pm 90°$ from ϕ_0. Otherwise, the patch is drawn in blue.

Figure 7 shows the phase distributions of flat surface of area 1.6 km by 1.6 km. The Kirchhoff simulator reproduces the Fresnel zone results as the regions with alternative yellow and blue colors corresponding to different Fresnel zones [20]. The phase distribution of DEM with noise $f_{DEM}(x,y) = d_i + n_i$ is plotted in Figure 8. With $f_{DEM}(x,y) = d_i + n_i$, the phase becomes randomly distributed indicating that the Fresnel zones of a flat surface disappear with the DEM. It is necessary to add the noise because the DEM is rounded to 1 meter which is 4 times of the wavelength causing phase changes of many pi's. The addition of noise is to avoid phase bias due to rounding to 1 meter.
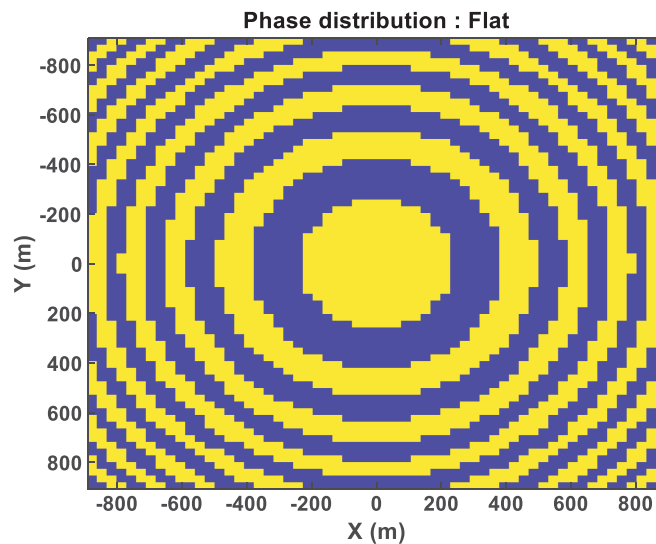
Figure 7. Phase distributions of flat surface showing Fresnel zones.
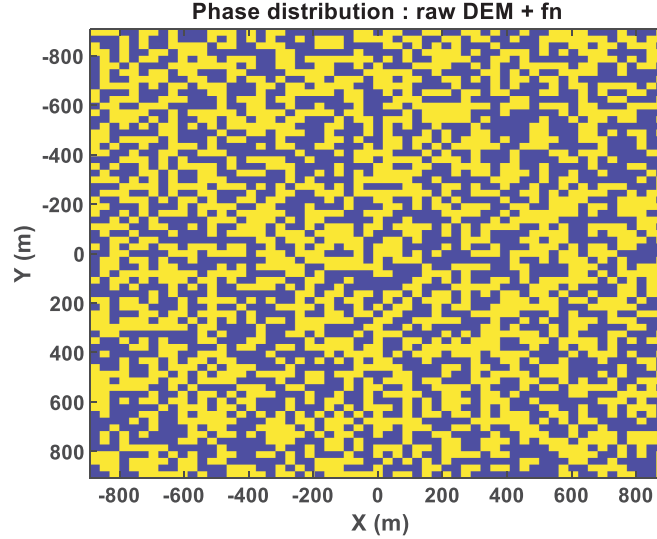
Figure 8. Phase distributions of surface with raw DEM + noise showing that the Fresnel zone concept is not valid.
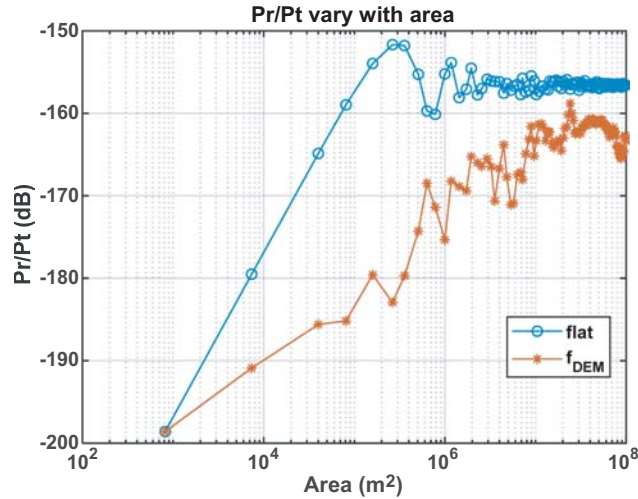
Figure 9. Power ratio as a function of area for flat and DEM surface at 1.575 GHz. For flat surface first Fresnel zone is twice of the final value. For the multiple elevation is only 2.5% of total. More multiple elevation results for the contribution of first Fresnel zone are shown in Table 5.

In Figure 9, we plot the power as a function of area around the specular point for the flat surface and for the surface with DEM. For the flat surface case, the major contributions come from the first few Fresnel zones. The coherent model is based on this concept of Fresnel zones. However, after including the DEM, the coherence within each Fresnel zone is destroyed as shown by the orange curve. The major contributions do not come from the first few Fresnel zones. The power gradually increases with the area. Thus the results of the DEM case are completely different from the flat surface case giving totally different interpretations.

4.3. Microwave Roughness Superimposed on DEM: $f(x,y) = f_{DEM}(x,y) + f_{mr}(x,y)$

These profiles can be assumed to be more representative of land surfaces. Three different DEM profiles of area 10 km by 10 km are selected, and the detailed information is listed in Table 4. As described earlier, the noise term n_i is added to the raw DEM. For the microwave roughness, a single realization

Table 4. Detailed information of DEM surface.

	Patch size (m × m)	Patch array size	Mean d (m)	d range (m)	Std d
DEM-1	26.53 × 30.81	377 × 325	120.67	[80, 163]	10.06
DEM-2	25.35 × 30.82	395 × 325	468.88	[402, 550]	20.79
DEM-3	30 × 30	333 × 333	111.46	[60, 167]	11.97
	STD d First Fresnel zone	Northwest	Northeast	Southwest	Southeast
DEM-1	5.53	31°45′17″N 83°43′48″W	31°45′17″N 83°37′32″W	31°38′41″N 83°43′48″W	31°38′41″N 83°37′32″W
DEM-2	7.59	35°39′35″N 98°27′0″W	35°39′35″N 98°20′26″W	35°34′11″N 98°27′0″W	35°34′11″N 98°20′26″W
DEM-3	5.76	31°49′52″N 83°49′52″W	31°49′52″N 83°44′20″W	31°44′20″N 83°49′52″W	31°44′20″N 83°44′20″E
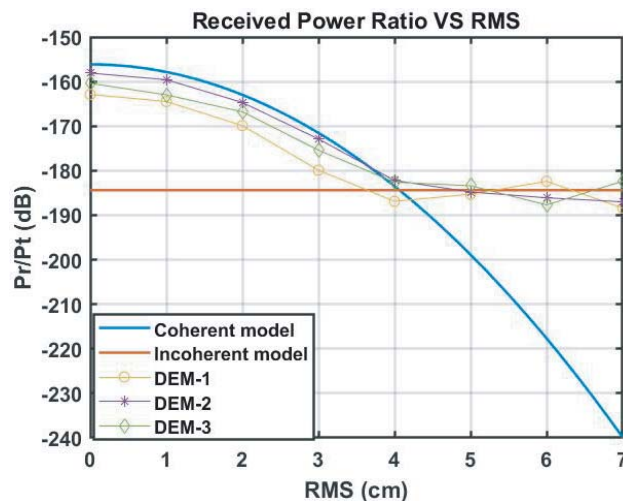
Figure 10. The overall rms height for multiple elevations are more than 10 meters as shown in Table 4. Each elevation has microwave roughness of centimeters. Results of Kirchhoff simulator, coherent model and incoherent model.

of microwave random rough surface is used with slope $s = 0.1$. Frequency average is taken within the 10 MHz bandwidth.

The power ratios calculated from KA simulator are plotted as a function of h up to 7 cm in Figure 10. The simulated results for h less than 4 cm are much greater than that of the incoherent model. The results with rms beyond 4 cm are close to that of the incoherent model. Note that Figure 10 is for the case of many elevations with the rms height elevations in meters. However, it is reasonable that the rms height at each elevation is less than 4 cm. For small microwave RMS heights, the Kirchhoff simulator gives results that are less or much less than the coherent model. The results in this figure show that the assumptions of both coherent model and incoherent model are not valid. Table 5 gives the fraction of power coming from the first Fresnel zone. The percentages are small for all three cases showing that the Fresnel zone concepts are inadequate for land surfaces with DEM.

Given the surface profiles, the numerical Kirchhoff simulator uniquely gives the results under the Kirchhoff approximation. The results, on the other hand, depend on the DEM descriptions. This is also consistent with Maxwell equations as Maxwell equations give a unique answer when the geometry of the surface profile is clearly defined.

Table 5. Power contribution from First Fresnel zone to total (averaged over Band width).

	Power from First Fresnel zone	Total power in $10\,\mathrm{km} \times 10\,\mathrm{km}$	Power ratio
DEM-1	$1752\,\mathrm{dB}$	$1629\,\mathrm{dB}$	5.9%
DEM-2	$171.0\,\mathrm{dB}$	$158.2\,\mathrm{dB}$	5.0%
DEM-3	$171.7\,\mathrm{dB}$	$160.4\,\mathrm{dB}$	7.4%

5. CONCLUSIONS

A distinct feature of GNSS-R land reflectometry is that the random rough surfaces are superimposed on many levels of elevation with the rms elevations in tens of meters which are many times larger than the microwave wavelength at GNSS frequencies. This is a new rough surface scattering problem as past rough surfaces scattering [20, 25–27] only treat rough surfaces on a single elevation. We studied this new problem using Kirchhoff integral as a first principle calculation. Using DEM without random microwave roughness, the Fresnel phase zones are destroyed, and power contributions come from areas much larger than the first few Fresnel zones. When microwave roughness is superimposed on DEM, the simulation results are much larger than the incoherent model and smaller than the coherent model for small RMS heights. In this study, the Gaussian correlation function is used. Numerical 3D solutions of Maxwell equations (NMM3D) for rough surface scattering have been calculated [22–24, 28] using exponential correlation functions. In past NMM3D simulations [22], we calculated both coherent and incoherent waves. We are presently combining the NMM3D with the numerical Kirchhoff simulator to develop a physical model for GNSS-R land applications. In the recent baseline active radar algorithm for SMAP, microwave roughness up to RMS height of 5 cm with exponential correlation function is used in the NMM3D data cubes [29]. Although the Kirchhoff approximation has limitations, the numerical Kirchhoff simulator gives a baseline reference model accounting the phase variations due to both elevations and microwave cm roughness.

APPENDIX A. COHERENT FIELD OF SPHERICAL WAVES SCATTERED BY RANDOM ROUGH SURFACE

The coherent fields of random rough surface were derived for plane waves [19]. In this appendix we derive coherent fields of spherical waves using spectral expansions and the method of stationary phase. We consider scalar waves below. The method can be readily extended to vector spherical waves for dielectric rough surface scattering. The geometrical configuration is as shown in Figure 1. The specular point is at $(0, 0)$. The horizontal separation between transmitter and receiver is L. The transmitter and receiver heights are respectively at h_t and h_r. The transmitter is at $(x_t, 0, h_t)$. The receiver is at $(x_r, 0, h_r)$, where

$$x_t = -\frac{L}{(h_r + h_t)} h_t \tag{A1a}$$

$$x_r = \frac{L}{(h_r + h_t)} h_r \tag{A1b}$$

The distance between transmitter and specular point is

$$R_t = \frac{h_t}{(h_r + h_t)} \sqrt{L^2 + (h_r + h_t)^2} \tag{A2a}$$

The distance between receiver and specular point is

$$R_r = \frac{h_r}{(h_r + h_t)} \sqrt{L^2 + (h_r + h_t)^2} \tag{A2b}$$

and

$$R_t + R_r = \sqrt{L^2 + (h_r + h_t)^2} \tag{A2c}$$

The incidence angle is

$$\theta_i = \cos^{-1}\left(\frac{(h_r + h_t)}{\sqrt{L^2 + (h_r + h_t)^2}}\right) \tag{A3}$$

In scalar Kirchhoff theory, we use Dirichlet boundary conditions. The rough surface coordinates are $(x'y'z')$, where $z' = f(x'y')$ is the roughness height function. The scattered field E_s is obtained by integration over the surface area

$$E_s = -2 \iint dS' g_0 \frac{\partial E_{inc}(r')}{\partial n'}$$

$$= -2 \iint dx' dy' g_0 \left(-\frac{\partial f}{\partial x'}\frac{\partial}{\partial x'} - \frac{\partial f}{\partial y'}\frac{\partial}{\partial y'} + \frac{\partial}{\partial z'}\right) E_{inc}(r') \tag{A4}$$

where the incident field $E_{inc}(r')$, in spatial and spectral domains, is

$$E_{inc} = 4\pi E_0 R_t \frac{\exp\left(ik\sqrt{(x'-x_t)^2 + (y)^2 + (z'-h_t)^2}\right)}{4\pi\sqrt{(x'-x_t)^2 + (y)^2 + (z'-h_t)^2}}$$

$$= 4\pi E_0 R_t \frac{i}{8\pi^2}\int_{-\infty}^{\infty} dk'_x \int_{-\infty}^{\infty} dk'_y \frac{\exp(ik'_x(x'-x_t) + ik'_y(y') + ik'_z(h_t - z'))}{k'_z} \tag{A5}$$

The Green's function, in spatial and spectral domains, is

$$g_0 = \frac{\exp\left(ik\sqrt{(x_r - x')^2 + y'^2 + (h_r - z')^2}\right)}{4\pi\sqrt{(x_r - x')^2 + y'^2 + (h_r - z')^2}}$$

$$= \frac{i}{8\pi^2}\int_{-\infty}^{\infty} dk_x \int_{-\infty}^{\infty} dk_y \frac{\exp(ik_x(x_r - x') + ik_y(-y') + ik_z(h_r - f(x',y')))}{k_z} \tag{A6}$$

In the above spectral expansions, $k_z = \sqrt{k^2 - k_x^2 - k_{y^2}}$. Substitution in Eq. (A5) and performing integration by Eqs. (A3), (A4), and (A6)

$$E_s = -2\iint dx' dy' \frac{i}{8\pi^2}\int_{-\infty}^{\infty} dk_x \int_{-\infty}^{\infty} dk_y \frac{\exp\left(ik_x(L + x_t - x') + ik_y(-y') + ik_z(h_r - f(x',y'))\right)}{k_z}$$

$$4\pi E_0 R_t \frac{1}{8\pi^2}\int_{-\infty}^{\infty} dk'_x \int_{-\infty}^{\infty} dk'_y \left(\frac{[(k'_x - k_x)]}{(k'_z + k_z)}k'_x + \frac{[(k'_y - k_y)]}{(k'_z + k_z)}k'_y + k'_z\right)$$

$$\frac{\exp(ik'_x(x' - x_t) + ik'_y(y') + ik'_z(h_t - f(x',)))}{k'_z} \tag{A7}$$

To calculate the coherent field, we take ensemble average over random roughness to calculate $\langle E_S \rangle$. Assuming that roughness is statistically homogenous, we have

$$\langle \exp\left(-i(k'_z + k_z) f(x',y')\right)\rangle = \exp\left(-\frac{(k'_z + k_z)^2 h^2}{2}\right) \tag{A8}$$

where h is the RMS height of random rough surface. Next we use

$$\iint dx' dy' \exp\left(i(k'_x - k_x) + i(k'_y - k_y) y'\right) = 4\pi^2 \delta(k_x - k'_x) \delta(k_y - k'_y) \tag{A9}$$

where δ is the Dirac delta function. Using delta functions, the integrations $\int_{-\infty}^{\infty} dk'_x \int_{-\infty}^{\infty} dk'_y$ are canceled. Then

$$\langle E_S \rangle = -\frac{i}{8\pi^2} 4\pi E_0 R_t \int_{-\infty}^{\infty} dk_x \int_{-\infty}^{\infty} dk_y \frac{\exp(ik_x L + ik_z(h_r + h_t))}{k_z}\exp\left(-2k_z^2 h^2\right) \tag{A10}$$

We calculate the above spectral integral using the method of stationary phase. At the stationary phase point,

$$k_z = \frac{(h_r + h_t)}{L} k_x = k \frac{(h_r + h_t)}{\sqrt{L^2 + (h_t + h_r)^2}} = k \cos \theta_i \tag{A11}$$

Then

$$\langle E_S \rangle = -E_0 R_t \exp\left(-2\left(k^2 \cos^2 \theta_i\right) h^2\right) \frac{\exp\left(ik\sqrt{L^2 + (h_r + h_t)^2}\right)}{\sqrt{L^2 + (h_r + h_t)^2}} \tag{A12}$$

The absolute value squared is

$$|\langle E_S \rangle|^2 = (E_0 R_t)^2 \exp\left(-4\left(k^2 \cos^2 \theta_i\right) h^2\right) \frac{1}{(R_t + R_r)^2} \tag{A13}$$

REFERENCES

1. Hall, C. and R. Cordey, "Multistatic scatterometry," *1988 International Geoscience and Remote Sensing Symposium, IGARSS'88, Remote Sensing: Moving Toward the 21st Century*, 561–562, 1988.

2. Martin-Neira, M., "A passive reflectometry and interferometry system (PARIS): Application to ocean altimetry," *ESA Journal*, Vol. 17, 331–355, 1993.

3. Garrison, J. L., S. J. Katzberg, and M. I. Hill, "Effect of sea roughness on bistatically scattered range coded signals from the Global Positioning System," *Geophysical Research Letters*, Vol. 25, 2257–2260, 1998.

4. Zavorotny, V. U. and A. G. Voronovich, "Scattering of GPS signals from the ocean with wind remote sensing application," *IEEE Transactions on Geoscience and Remote Sensing*, Vol. 38, 951–964, 2000.

5. Fabra, F., E. Cardellach, A. Rius, S. Ribo, S. Oliveras, O. Nogués-Correig, et al., "Phase altimetry with dual polarization GNSS-R over sea ice," *IEEE Transactions on Geoscience and Remote Sensing*, Vol. 50, 2112–2121, 2012.

6. Larson, K. M., E. D. Gutmann, V. U. Zavorotny, J. J. Braun, M. W. Williams, and F. G. Nievinski, "Can we measure snow depth with GPS receivers?," *Geophysical Research Letters*, Vol. 36, 2009.

7. Gleason, S., M. Adjrad, and M. Unwin, "Sensing ocean, ice and land reflected signals from space: Results from the UK-DMC GPS reflectometry experiment," *Proceedings of the 2005 ION GNSS Technical Meeting*, 13–16, 2005.

8. Zavorotny, V. U., S. Gleason, E. Cardellach, and A. Camps, "Tutorial on remote sensing using GNSS bistatic radar of opportunity," *IEEE Geoscience and Remote Sensing Magazine*, Vol. 2, 8–45, 2014.

9. Ruf, C., P. Chang, M. Clarizia, S. Gleason, Z. Jelenak, J. Murray, et al., *CYGNSS Handbook*, Ann Arbor, MI, Michigan Pub., ISBN, 978-1, 2016.

10. Clarizia, M. P. and C. S. Ruf, "Wind speed retrieval algorithm for the Cyclone Global Navigation Satellite System (CYGNSS) mission," *IEEE Transactions on Geoscience and Remote Sensing*, Vol. 54, 4419–4432, 2016.

11. Ruf, C. S., S. Gleason, and D. S. McKague, "Assessment of CYGNSS wind speed retrieval uncertainty," *IEEE Journal of Selected Topics in Applied Earth Observations and Remote Sensing*, 2018.

12. Chew, C., R. Shah, C. Zuffada, G. Hajj, D. Masters, and A. J. Mannucci, "Demonstrating soil moisture remote sensing with observations from the UK TechDemoSat-1 satellite mission," *Geophysical Research Letters*, Vol. 43, 3317–3324, 2016.

13. Camps, A., H. Park, M. Pablos, G. Foti, C. P. Gommenginger, P.-W. Liu, et al., "Sensitivity of GNSS-R spaceborne observations to soil moisture and vegetation," *IEEE Journal of Selected Topics in Applied Earth Observations and Remote Sensing*, Vol. 9, 4730–4742, 2016.

14. Kim, H. and V. Lakshmi, "Use of Cyclone Global Navigation Satellite System (CYGNSS) observations for estimation of soil moisture," *Geophysical Research Letters*, Vol. 45, 8272–8282, 2018.

15. Carreno-Luengo, H., G. Luzi, and M. Crosetto, "Sensitivity of CyGNSS bistatic reflectivity and SMAP microwave radiometry brightness temperature to geophysical parameters over land surfaces," *IEEE Journal of Selected Topics in Applied Earth Observations and Remote Sensing*, 1–16, 2018.

16. Chew, C., J. T. Reager, and E. Small, "CYGNSS data map flood inundation during the 2017 Atlantic hurricane season," *Scientific Reports (Nature Publisher Group)*, Vol. 8, 1–8, 2018.

17. Chew, C., A. Colliander, R. Shah, C. Zuffada, and M. Burgin, "The sensitivity of ground-reflected GNSS signals to near-surface soil moisture, as recorded by spaceborne receivers," *2017 IEEE International Geoscience and Remote Sensing Symposium, IGARSS 2017*, 2661–2663, 2017.

18. Al-Khaldi, M., J. Johnson, A. O'Brien, F. Mattia, and A. Balenzano, "GNSS-R time-series soil moisture retrievals from vegetated surfaces," in *2018 IEEE International Geoscience and Remote Sensing Symposium, IGARSS 2018*, 2035–2038, 2018.

19. Tsang, L. and J. Kong, *Scattering of Electromagnetic Waves, Vol. 3: Advanced Topics*, 413, Wiley Interscience, 2001.

20. Beckmann, P. and A. Spizzichino, *The Scattering of Electromagnetic Waves from Rough Surfaces*, 511, Artech House, Inc., Norwood, MA, 1987.

21. Tsang, L., J. Kong, and K. Ding, *Scattering of Electromagnetic Waves, Vol. 1: Theory and Applications*, Wieley Interscience, New York, 2000.

22. Huang, S., L. Tsang, E. G. Njoku, and K. S. Chan, "Backscattering coefficients, coherent reflectivities, and emissivities of randomly rough soil surfaces at L-band for SMAP applications based on numerical solutions of maxwell equations in three-dimensional simulations," *IEEE Transactions on Geoscience and Remote Sensing*, Vol. 48, 2557–2568, 2010.

23. Huang, S. and L. Tsang, "Electromagnetic scattering of randomly rough soil surfaces based on numerical solutions of Maxwell equations in three-dimensional simulations using a hybrid UV/PBTG/SMCG method," *IEEE Transactions on Geoscience and Remote Sensing*, Vol. 50, 4025–4035, 2012.

24. Liao, T.-H., L. Tsang, S. Huang, N. Niamsuwan, S. Jaruwatanadilok, S.-B. Kim, et al., "Copolarized and cross-polarized backscattering from random rough soil surfaces from L-band to Ku-band using numerical solutions of Maxwell's equations with near-field precondition," *IEEE Transactions on Geoscience and Remote Sensing*, Vol. 54, 651–662, 2016.

25. Ishimaru, A., *Wave Propagation and Scattering in Random Meida*, Vol. 1 and Vol. 2, Academic Press, New York, 1978.

26. Tsang, L., J. A. Kong, and R. T. Shin, *Theory of Microwave Remote Sensing*, John Wiley&Sons, New York, 1985.

27. Fung, A. K., *Microwave Scattering and Emission Models and Their Applications*, Artech House, Boston, 1994

28. Chen, K.-S., L. Tsang, K.-L. Chen, T. H. Liao, and J.-S. Lee, "Polarimetric simulations of SAR at L-band over bare soil using scattering matrices of random rough surfaces from numerical three-dimensional solutions of Maxwell equations," *IEEE Transactions on Geoscience and Remote Sensing*, Vol. 52, 7048–7058, 2014.

29. Kim, S.-B., J. J. Van Zyl, J. T. Johnson, M. Moghaddam, L. Tsang, A. Colliander, et al., "Surface soil moisture retrieval using the L-band synthetic aperture radar onboard the soil moisture active-passive satellite and evaluation at core validation sites," *IEEE Transactions on Geoscience and Remote Sensing*, Vol. 55, 1897–1914, 2017.